

Light Element Abundances and Multiple Populations in M53

Jeffrey M. Gerber, Eileen D. Friel, and Enrico Vesperini Department of Astronomy, Indiana University Bloomington, Swain West 319, 727 East 3rd Street, Bloomington, IN 47405-7105, USA Received 2020 September 25; revised 2021 March 14; accepted 2021 March 16; published 2021 May 28

Abstract

We present results from a study of 94 red giant stars in the globular cluster M53. We use low-resolution spectra to measure the strength of CN and CH features at \sim 3800 and 4300 Å, respectively. The strengths of these features are used to classify stars into a CN-enhanced and CN-normal population and to measure C and N abundances in all 94 stars. We find the red giant branch stars to be evenly split between the two populations identified, and observe the presence of CN-enhanced stars on the asymptotic giant branch. In addition, we identify five CH star candidates based on the strength of their CN and CH band features, and the presence of a P-branch in their CH band. We compare our identification of multiple populations to those based on the Na-O anticorrelation and pseudo-color indices in Hubble Space Telescope UV photometry, and find general agreement between all three methods. Our large sample size also allows us to study the radial distribution of each population, and we find that the CNenhanced population is more centrally concentrated. We use our C and N measurements to compare the evolutionary changes in these elements as a function of magnitude between the two populations, and show that both populations experience similar evolutionary changes to the surface abundances of C and N. Finally, we calculate C+N+O abundances for each population and compare them to similar measurements made in M10; we find that in both clusters, CN-enhanced stars have a slightly enhanced C+N+O (Δ (C+N+O) \sim 0.2 dex).

Unified Astronomy Thesaurus concepts: Globular star clusters (656); Stellar evolution (1599); Stellar abundances (1577)

Supporting material: machine-readable table

1. Introduction

As some of the oldest objects in the Milky Way, globular clusters (GCs) are important to better our understanding of topics such as Galactic formation and evolution, Galactic dynamical history, and low-mass stellar evolution. Numerous studies have revealed a picture of GCs much more complex than that according to which these systems would be composed of chemically homogeneous stars all formed from the same material. Early spectroscopic studies of red giant branch (RGB) stars showed the presence in a few GCs of inhomogeneities in light element abundances such as carbon (C), nitrogen (N), oxygen (O), sodium (Na), aluminum (Al), and magnesium (Mg). After decades of study, it is now known that these inhomogeneities in RGB stars are caused by two phenomena: multiple populations of stars in GCs and noncanonical, deep mixing in late-stage RGB stars (Kraft 1994; Gratton et al. 2012, and references therein). Spectroscopic and photometric investigations in the last two decades have provided strong evidence of the presence of multiple stellar populations in all of the GCs studied (see, e.g., the recent reviews by Bastian & Lardo 2018; Gratton et al. 2019, and references therein).

Notably, spectroscopic studies have demonstrated the existence on C-N, Na-O, and Mg-Al anticorrelations in all evolutionary stages in all Galactic GCs that have been studied, which indicates the existence of multiple populations of stars with different light element abundances (see, e.g., Gratton et al. 2012, and references therein). More recent studies using Hubble Space Telescope (HST) UV photometry have also indicated the presence of multiple populations in every GC observed (Piotto et al. 2015; Milone et al. 2017). In the majority of GCs, these populations differ only in light element abundances, which indicates that the progenitors that provided the intracluster material to form the additional populations did

not enhance the heavy elements such as Fe. 1 This observation leaves only a few possible scenarios to create multiple populations, which are still heavily debated. Current candidates for the progenitor stars include massive asymptotic giant branch (AGB) stars (see, e.g., Ventura et al. 2001; D'Ercole et al. 2008, 2012), fast rotating massive stars (Prantzos & Charbonnel 2006; Decressin et al. 2007b), massive binary stars (de Mink et al. 2009), and supermassive stars (Denissenkov & Hartwick 2014; Elmegreen 2017; Gieles et al. 2018). All of these candidates would eject material slowly enough to be captured by the gravitational potential of the GC, and go through nucleosynthesis processes that could explain the anticorrelations observed such as the CN(O)-cycle and Ne-Na

In addition to initial differences in C and N caused by multiple populations, low-mass, low-metallicity RGB stars in GCs have been observed to go through an evolutionary process that causes additional C-depletion and N-enhancement to their surface abundances. This process, often referred to as "extra" or "secondary" mixing, takes place in RGB stars after they have passed a point on the color–magnitude diagram (CMD) called the luminosity function bump (LFB). The LFB is a result of canonical stellar evolution in RGB stars. When the expanding hydrogen (H) burning shell reaches a chemical weight difference (the μ -barrier), the shell is given an influx of H causing the star to burn bluer for a brief moment before equilibrium is reestablished and the star once again continues its ascent up the RGB. As multiple RGB stars ascend, then

About 15% of the GCs studied show even more complex chemical properties including variations in heavy elements; some of these GCs may be the cores of tidally disrupted dwarf galaxies accreted and, more in general, the formation history of these systems must include the additional contribution of progenitors enriching the cluster with heavy elements; see, e.g., Johnson et al. (2015b), Marino et al. (2015), Yong et al. (2015), and Da Costa (2016).

descend, then ascend once again, the result is a "bump" in the luminosity function caused by multiple stars passing one another on the same point in the CMD. After RGB stars have passed this evolutionary stage, the μ -barrier no longer prevents material from the H-burning envelope from transferring into the outer convective envelope and being transported to the surface. Because this material has gone through the CN(O)-cycle, it is depleted in C, enhanced in N, and enhanced in C13, which causes the observed changes in surface abundances of C, N, and ¹²C/¹³C. However, the exact mechanism that causes this material to be transported between the H-burning envelope and the convective envelope is still not very well understood. Some of the main candidates include thermohaline mixing (Kippenhahn et al. 1980; Eggleton et al. 2006, 2008; Charbonnel & Zahn 2007; Henkel et al. 2017), rotational instability driven mixing (Sweigart & Mengel 1979; Chanamé et al. 2005; Palacios et al. 2006), magnetic fields (Hubbard & Dearborn 1980; Busso et al. 2007; Nordhaus et al. 2008; Palmerini et al. 2009), and internal gravity waves (Denissenkov & Tout 2000), but no theory is currently able to match all observations without additional corrections.

For the following study, we focused on providing new observations to better understand these two phenomena through C and N abundances in the RGB stars of the lowmetallicity GC, M53 (NGC 5024). Because both primordial chemical differences in the multiple populations present in GCs and secondary mixing will affect the surface abundances through CN(O)-cycle material, it can be difficult to separate the two effects when studying C and N in RGB stars. In order to disentangle this degeneracy in the possible origin of the variations in the surface abundances, we have observed a large number of stars (\sim 100) covering a wide range of magnitudes from the tip of the RGB down to just below the LFB. We determine C and N abundances for the stars in our sample using low-resolution spectroscopy to measure CN and CH molecular features in the near-UV. We then use the strengths of these features and the C and N abundances to classify stars into different populations, and measure the change in surface abundances as a function of magnitude.

This work follows our similar studies of M10 (Gerber et al. 2018, hereafter G18) and M71 (Gerber et al. 2020, hereafter G20). M53 is the low-metallicity cluster in this series with an [Fe/H] of -2.07 dex (Boberg et al. 2016). Normally, CN bands are too weak to detect multiple populations in clusters of such a low metallicity, yet a previous study of a small sample of RGB stars in M53 found that the width of the distribution in CN band strengths exceeded the uncertainties, which indicated the presence of multiple populations (Martell et al. 2008b). M53 also has Na and O abundance measurements from Boberg et al. (2016), which can be used to make comparisons between classifications based on N, Na, and O. We can also make comparisons to the metal-poor clusters M92 and M15, which have relatively large sample sizes of C abundance measurements in the literature (see Smith & Martell 2003; Trefzger et al. 1983).

Results from recent studies also highlight why M53 and its unusually nearby neighbor cluster, NGC 5053, are an important and unique pair of GCs to study. A potential tidal stream associated with NGC 5053 was observed by Lauchner et al. (2006), which was later confirmed by Jordi & Grebel (2010). Chun et al. (2010) found evidence of a tidal bridge-like feature through wide field photometry between M53 and NGC 5053;

however, this finding was not confirmed by Jordi & Grebel (2010). Forbes & Bridges (2010) also suggested that M53 or NGC 5053 may be the remnant nucleus of a possible dwarf galaxy, although they mentioned that more data such as proper motions were needed to confirm this suggestion. Since these results, proper motions from Gaia have revealed that the two clusters are likely on similar orbital trajectories, which provided more evidence that this pair may be an interacting pair of clusters (Vasiliev 2019). In addition, a recent study by Yuan et al. (2020) has found evidence of a stream associated with M53 and NGC 5053 (see also Naidu et al. 2020) and suggested that M53 may be the core of a disrupted dwarf galaxy, which would provide an explanation as to how a pair of clusters at a small distance from each other formed so far away from the Galactic center. Further evidence suggesting that M53 and NGC 5053 are a pair of clusters associated with the remnants of an accreted dwarf galaxy has also been presented by Chun et al. (2020). These recent findings make it even more important to study M53 and better understand its overall formation history.

The C and N abundances of M53 have not been well studied previously; the analysis of 85 RGB stars and nine AGB stars presented in this paper provides a significant extension in the study of the chemical properties of this cluster. In Section 2, we describe our observations and data reduction methods. We discuss the band measurements and calculations of C and N abundances for all stars in the sample in Section 3. Section 4 discusses the relative proportions of first- and second-generation stars in our sample, the spatial distribution for the separate populations, a comparison with other identification methods, the evolution of C and N with magnitude, and a comparison to other clusters of similar metallicity (namely, M92 and M15). Our results and conclusions are summarized in Section 5.

2. Observations

2.1. Target Selection and Data Reduction

We completed our observations over three observing runs on the WIYN 2 3.5 m telescope during 2016 June 9–12, 2017 May 29–June 1, and 2018 April 22–24. We used the blue fibers of the Hydra multi-object spectrograph, which allows us to observe the near-UV CN band at 3883 Å and the CH band at 4300 Å.

To acquire spectra of many stars with similar signal-to-noise ratios (S/Ns) using Hydra, it is best to observe stars in a configuration with a luminosity range of no more than three magnitudes. For this reason, our configurations for observations of M53 were divided into "bright" and "faint" setups. Our bright setups ranged in magnitude from 13.5 < V < 16, and our faint setups from 15.5 < V < 17.5. This allowed us to observe stars as faint as the LFB at V = 16.49 (Nataf et al. 2013), which is the crucial point where extra mixing begins in RGB stars. The magnitude range of our sample can be seen in Figure 1, which is a CMD of M53 using photometry from Rey et al. (1998).

While selecting stars for our sample, we focused on observing stars with Na and O abundances from Boberg et al. (2016). Observing stars with measured Na and O

The WIYN Observatory is a joint facility of the University of Wisconsin-Madison, Indiana University, the National Optical-Infrared Astronomy Research Laboratory, the University of Missouri, Purdue University, Penn State University, and the University of California, Irvine.

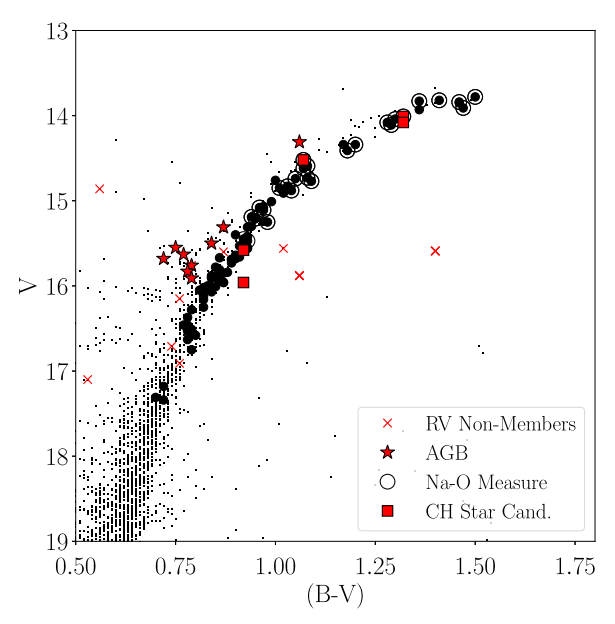


Figure 1. CMD of M53 using *B* and *V* photometry from Rey et al. (1998). Black circles and red stars indicate observed RGB and AGB member stars, respectively. Red "x" symbols indicate stars that were determined to be nonmembers based on their RVs. Red squares are CH star candidates as discussed in Section 4.2. Stars with Na or O abundance measurements from Boberg et al. (2016) are indicated.

abundances provides us with the ability to compare our classification method using CN band measurements and the method using the Na–O anticorrelation (see, e.g., Carretta et al. 2009a, 2009b). These comparisons are important as they can provide constraints on the progenitors for possible scenarios that lead to the formation of multiple populations. The O abundances also allow us to determine C and N abundances with higher accuracy as the balance between CN and CO molecular formation in a stellar atmosphere has a significant effect on the strength of the observed CN molecular feature.

Once observations were complete, our observed spectra were reduced using the IRAF³ package, dohydra. With dohydra, a one-dimensional spectrum is produced by tracing and extracting the light from each of the apertures from bias-subtracted images. Then the extracted spectra are flat-fielded, dispersion corrected, and sky-subtracted. Observations of a CuAr comparison lamp were used for dispersion correction. We then median-combined multiple observations of the same configuration using the IRAF package, scombine, to increase the S/N and reduce the effects of cosmic rays.

We used the "600@10.1" grating, which resulted in final spectra with a wavelength range of \sim 3750–6300 Å and an FWHM of \sim 4.5 Å. This telescope setup and reduction procedure is similar to what was used in G18 and G20 to collect the data sets in M10 and M71. The minimum S/N at the position of the CN band at 3883 Å is 20 and can be as high as 50 in some spectra with a typical S/N being \sim 30. The S/N at the position of the CH band (4300 Å) is much higher, with the lowest value observed being 100 and some spectra having an S/N as high as 200. A typical S/N value is \sim 150.

2.2. Radial Velocities and Membership Selection

We initially selected likely members to observe based on their location on the cluster CMD. Once observations were complete, we then used radial velocity (RV) measurements to further ensure that the stars were cluster members. RV measurements were made by cross-correlating absorption lines in the observed stellar spectra with a spectrum of an RV standard using the IRAF package, *fxcor*. We chose to use HD107328, HD109358, and HD132737 as RV standards as all three stars have a similar temperature and luminosity as the program stars. Observations of the three RV standards were made during each observing run. Uncertainties for individual measurements using this method at this resolution are around 15 km s⁻¹.

Our initial sample included 148 individual spectra. Forty-one measurements of multiple stars were included in the M53 sample, and these measurements were used to check for any offsets between nights or observing runs; none were found. To constrain membership, any stars with RVs above or below three standard deviations of the median were determined to be nonmembers and removed from the sample. This limit resulted in nine stars being classified as nonmembers based on RV. The final sample for M53 includes 85 RGB and nine AGB stars; these are shown in Figure 1 along with nonmembers and stars with Na or O abundances. We find a median RV of -60 ± 9 (std) km s⁻¹, which agrees with the values found by Boberg et al. $(2016; -63.2 \pm 0.5 \,\mathrm{km \, s^{-1}})$ and Kimmig et al. (2015; $-62.8 \pm 0.3 \,\mathrm{km \, s}^{-1}$) from higher-resolution data. A full list of objects observed, including RV nonmembers, is presented in Table 1.

3. Analysis

3.1. CN and CH Bands

3.1.1. Index Definitions

To measure the CN and CH molecular features, we made use of indices that create a "magnitude" of band strength by comparing the integrated flux of a feature bandpass to one or more continuum bandpasses. CN and CH indices have been used in many studies to identify multiple populations and measure C and N abundances in stars in GCs (e.g., Norris & Freeman 1979; Harbeck et al. 2003; Briley et al. 2004b; Smolinski et al. 2011).

Our index definitions were chosen such that they would be accurate for the large range of magnitudes (meaning large ranges in effective temperatures and surface gravities) that our sample covers. As in G18 and G20, we use the S(3839) and CH(4300) (referred to as CH throughout the rest of this paper) bands defined by Harbeck et al. (2003). This S(3839) index is based on the S(3839) index defined by Norris et al. (1981) with the difference being slightly tighter feature and continuum bandpass windows to avoid contamination from stronger Balmer lines in the fainter/warmer stars. The CH index is based on a similar index used by Cohen (1999a, 1999b) with continuum bandpasses chosen to avoid strong absorption by $H\gamma$ in warmer stars. Our final band definitions are:

$$S(3839) = -2.5 \log \frac{F_{3861-3884}}{F_{3894-3910}} \tag{1}$$

³ IRAF is distributed by the National Optical-infrared Astronomy Research Laboratory, which is operated by the Association of Universities for Research in Astronomy under cooperative agreement with the National Science Foundation.

$$CH = -2.5 \log \frac{F_{4285-4315}/30}{0.5(F_{4240-4280}/40) + 0.5(F_{4390-4460}/70)}$$
(2)

where F_{x-y} is the integrated flux between the wavelengths x and y in \mathring{A} .

3.1.2. Flux Calibration

We used the same method described in G18 and G20 to flux calibrate the spectra using model spectra generated by the synthetic spectrum generator (SSG; Bell et al. 1994, and references therein) using MARCS model atmospheres (Gustafsson et al. 2008). We used the average cluster metallicity of [Fe/H] = -2.07 from Boberg et al. (2016), and calculated effective temperatures from the V-K colors of the stars based on the method by Alonso et al. (1999, 2001) with V magnitudes from Rey et al. (1998) and K magnitudes from the Two Micron All Sky Survey (2MASS; Skrutskie et al. 2006). K magnitudes were corrected to the Carlos Sánchez Telescope system (Alonso et al. 1998) following the method by Johnson et al. (2005). If a star did not have a K magnitude, the relation for effective temperature based on B-V color was used (Alonso et al. 1999). To correct for extinction, a reddening correction of E(B-V) = 0.02 (Rey et al. 1998) was used for all stars in the cluster.

Surface gravities were calculated using the bolometric corrections given by Alonso et al. (1999) and are listed with the effective temperature for each star in Table 1. Absolute magnitudes were calculated for each star using an apparent distance modulus of $(m-M)_V = 16.32$ (Harris 1996; 2010 edition). These are also given in Table 1.

Using these stellar parameters, we created a scaled-solar spectrum for each star in the sample using the SSG. Each observed spectrum was divided by a corresponding scaled-solar spectrum matching its stellar parameters. The resulting ratio was then fit with a spline to create a function fitting the approximate instrumental response for a given spectrum. Each observed spectrum was then divided by the instrumental response function of that star to generate our sample of spectra with continua that had been calibrated to the models. For more details on this method, see G18.

3.1.3. Band Measurements

We measured S(3839) and CH index values using the flux-calibrated spectra for all of the stars in our sample for M53. These measurements are plotted vs. effective temperature in Figure 2 and listed in Table 1. Error bars in Figure 2 represent the calculated uncertainties for each band. Using multiple measurements of the same stars, we found that the S(3839) and CH band indices for stars in our sample have uncertainties of 0.05 and 0.01, respectively.

Figure 2 shows that both bands increase in strength as a function of decreasing effective temperature. While there is a spread in the S(3839) index measurements indicative of more than one population, the S(3839) index does not clearly separate into two populations except at the coolest temperatures, which is likely due to the extremely low metallicity of M53. Since the stars in this cluster are so metal poor, the CN bands are weaker in their spectra, which reduces any visible differences between populations that may exist. Therefore, to

better quantify whether a star is CN-enhanced or CN-normal, we used an objective classification method.

As in G18 and G20, our method involves defining a δ CN index by modeling and removing the changes in CN band strength as a function of effective temperature from our S(3839) index measurements. We model these changes using C and N abundance measurements made using our S(3839) and CH index measurements. To measure C and N in our stars, we use the SSG following the methods of Briley et al. (2004a, 2004b). Synthetic spectra are generated for each star with the effective temperature and surface gravity that was determined in Section 3.1.2 and given in Table 1, and an assumed initial C and N abundance. Then, the S(3839) and CH indices are measured in the synthetic spectrum, and the C and N abundances are simultaneously varied until the synthetic S(3839) and CH indices match what is observed.

Other than initial C and N abundances, we also assumed a microturbulence of 2.0 km s^{-1} and a C^{12}/C^{13} ratio of 4.0, which are representative of RGB stars in GCs (e.g., Suntzeff & Smith 1991; Pavlenko et al. 2003). For accurate models, we also have to assign an oxygen abundance for each star due to the dependence of CN and CH band strength on CO molecular formation in a star's atmosphere. We use an average [O/Fe] value for the cluster of 0.4 dex based on the measurements from Boberg et al. (2016). This assumption works for the purposes of these preliminary measurements, as the main goal is to determine the average C and N abundances as a function of luminosity.

The stellar C and N abundances were used to determine the average C and N abundance at 100 K intervals. Using these average abundances, we created average S(3839) and CH index measurements over the same intervals by measuring synthetic spectra created with the SSG. A spline was then fitted to these points, and used as a dividing line between the two populations; see the red lines in Figure 2. These lines represent the average S(3839) or CH index measurement for a given effective temperature. The δ CN index was calculated by subtracting the fit to the average at that effective temperature from the measured S(3839) value. Our definitions for each population match those from G18 and G20, with CN-enhanced stars having δ CN \leq 0.0. In Figure 2, CN-enhanced stars are indicated as filled points, and CN-normal stars are indicated as open points.

We also identify in Figure 2 five stars with abnormally high S(3839) measurements; all also have enhanced CH strengths. The δ CN index measured for these stars is almost twice as high as the next highest value of a CN-enhanced star, suggesting they have special properties. We defer a discussion of these stars, which we identify as potential CH stars, until Section 4.2, but label them as red squares in all figures so their behavior within the sample can be distinguished. We also present, for completeness, our calculated abundance values for each of these CH star candidates, and include them with the caveat that our analysis technique may not be capable of producing truly accurate values for stars with such extreme CN and CH molecular features.

3.2. Determining C and N Abundances

To determine our final C and N abundances for each star, we follow the same method described above to find initial abundances. The only difference in our final abundances is that once the stars are classified into populations, more specific

Table 1 Stars Measured in M53

								Demo marc	The same								
\mathbb{ID}^a	R.A. ^a	Decl. ^a	$\frac{\mathrm{RV}_{\mathrm{hel}}}{\mathrm{km s}^{-1}}$	$V^{\mathbf{a}}$	$M_{\rm V}^{ m b}$	$K_{\rm 2MASS}$	$T_{ m eff}$	$\frac{\log g}{(\operatorname{cm s}^{-1})}$	S(3839)	δCN	СН	[C/Fe]	[N/Fe]	$[{ m O/Fe}]^{ m c}$	[Na/Fe] ^c	Branch	Memb
	(000=6)	(000=0)	((Smir)	(9,)	(9,)		(5 ma)									
4	198.191361	18.191845	-54	13.78	-2.54	10.441	4048	89.0	-0.118	0.082	0.279	-0.68	1.71	0.4	0.5	RGB	y
7	198.238318	18.149578	09-	13.82	-2.50	13.640	4067	0.71	-0.075	0.120	0.303	-0.57	1.58	0.1	0.4	RGB	y
6	198.253564	18.167292	09-	13.83	-2.49	13.445	4119	92.0	-0.270	-0.084	0.289	-0.61	1.13	-0.1	0.4	RGB	y
10	198.232289	18.189502	-54	13.84	-2.48	10.514	4055	0.71	-0.265	-0.067	0.297	-0.57	1.20	-0.2	0.5	RGB	y
12	198.233857	18.139113	-26	13.85	-2.47	10.522	4054	0.71	-0.067	0.131	0.275	-0.75	1.80	:	÷	RGB	y
14	198.268107	18.182968	-53	13.91	-2.41	10.707	4124	0.79	-0.235	-0.050	0.278	-0.51	1.35	0.0	0.7	RGB	'n
15	198.211288	18.161073	-53	13.93	-2.39	10.719	4119	0.80	-0.130	0.056	0.261	-0.77	1.64	:	÷	RGB	y
18	198.210175	18.178769	-53	14.01	-2.31	13.039	4162	98.0	0.080	0.262	0.348	-0.31	1.55	0.2	0.4	CH Star Cand.	y
20	198.235309	18.144363	-26	14.04	-2.28	10.974	4208	0.91	-0.263	-0.082	0.290	-0.46	1.07	-0.2	0.5	RGB	y
26	198.251358	18.168852	-72	14.08	-2.24	14.115	4162	0.89	0.187	0.369	0.462	0.13	1.18	:	:	CH Star Cand.	y
28	198.218386	18.173816	-57	14.08	-2.24	12.446	4207	0.92	-0.079	0.102	0.280	-0.61	1.52	0.3	0.3	RGB	y
29	198.209281	18.149267	-59	14.11	-2.21	11.001	4181	0.92	-0.147	0.034	0.296	-0.47	1.36	-0.2	0.5	RGB	y
38	198.261212	18.184932	-61	14.31	-2.01	11.497	4383	1.13	-0.312	-0.112	0.227	-0.63	1.16	:	:	AGB	y
39	198.198274	18.169346	-77	14.34	-1.98	11.469	4340	1.12	-0.162	0.031	0.253	-0.59	1.41	:	:	RGB	y
40	198.203296	18.238325	-64	14.34	-1.98	11.367	4269	1.07	-0.261	-0.076	0.292	-0.41	1.05	0.0	0.5	RGB	'n
4	198.183393	18.170152	99-	14.41	-1.91	11.505	4317	1.13	-0.253	-0.063	0.305	-0.32	0.99	-0.2	0.5	RGB	'n
47	198.233739	18.185220	49–	14.52	-1.80	11.709	4385	1.22	0.035	0.236	0.300	-0.43	1.51	0.3	0.1	CH Star Cand.	S
53	198.201814	18.213504		14.59	-1.73	11.808	4407	1.26	-0.197	0.008	0.243	-0.58	1.35	0.0	0.3	RGB	y
54	198.270264	18.247453	-62	14.62	-1.70	11.940	4488	1.32	-0.300	-0.078	0.260	-0.35	1.02	0.0	0.5	RGB	y
09	198.236786	18.100674	-26	14.73	-1.59	12.073	4507	1.38	-0.150	0.076	0.245	-0.47	1.42	0.3	0.2	RGB	y
61	198.231885	18.220191	<i>L</i> 9–	14.74	-1.58	12.111	4531	1.40	-0.254	-0.023	0.283	-0.24	1.06	0.0	0.4	RGB	y
2	198.253228	18.200100	40-	14.76	-1.56	11.997	4422	1.34	-0.281	-0.073	0.188	-0.80	1.48	:	÷	RGB	y
65	198.152838	18.126203	09-	14.77	-1.55	13.076	4430	1.35	-0.232	-0.023	0.297	-0.30	1.05	-0.1	0.4	RGB	y
89	198.259119	18.222985	-58	14.83	-1.49	12.188	4520	1.43	-0.302	-0.074	0.266	-0.29	1.02	0.0	0.5	RGB	y
70	198.201253	18.238394	-65	14.85	-1.47	12.198	4511	1.43	-0.315	-0.088	0.227	-0.53	1.12	0.0	0.3	RGB	y
72	198.199614	18.109783	-59	14.88	-1.44	12.230	4513	1.44	-0.307	-0.080	0.257	-0.40	1.01	0.0	0.3	RGB	y
77	198.262790	18.195211	-62	14.91	-1.41	12.153	4426	1.40	-0.181	0.028	0.215	-0.68	1.55	:	:	RGB	y
84	198.287056	18.188487	69-	15.01	-1.31	÷	4558	1.52	-0.194	0.044	0.236	-0.40	1.39	:	:	RGB	y
98	198.227725	18.092297	-58	15.08	-1.24	12.615	4672	1.61	-0.134	0.129	0.251	-0.16	1.50	0.0	0.5	RGB	y
87	198.208583	18.197453	09-	15.08	-1.24	12.484	4559	1.55	-0.361	-0.124	0.238	-0.37	0.92	:	:	RGB	y
91	198.207839	18.187731	-74	15.11	-1.21	15.192	4585	1.57	-0.235	0.008	0.230	-0.39	1.34	0.1	0.4	RGB	y
95	198.241690	18.153194	-59	15.19	-1.13	14.510	4625	1.63	-0.207	0.045	0.216	-0.42	1.45	0.2	0.2	RGB	y
26	198.235564	18.210077	-62	15.21	-1.11	12.653	4579	1.61	-0.189	0.053	0.224	-0.48	4.	0.0	0.1	RGB	y
66	198.264958	18.148353	-58	15.24	-1.08	15.069	4585	1.63	-0.237	900.0	0.279	-0.21	1.14	:	:	RGB	Y
101	198.149573	18.241642	09-	15.25	-1.07	:	4571	1.62	-0.273	-0.033	0.290	-0.17	1.00	0.1	0.4	RGB	y

Notes. Only a portion of this table is shown here to demonstrate its form and content. A machine-readable version of the full table is available.

(This table is available in its entirety in machine-readable form.)

^a Rey et al. (1998).

^b Assumes $(m-M)_v = 16.32$ (Harris 1996; 2010 edition).

^c Boberg et al. (2016).

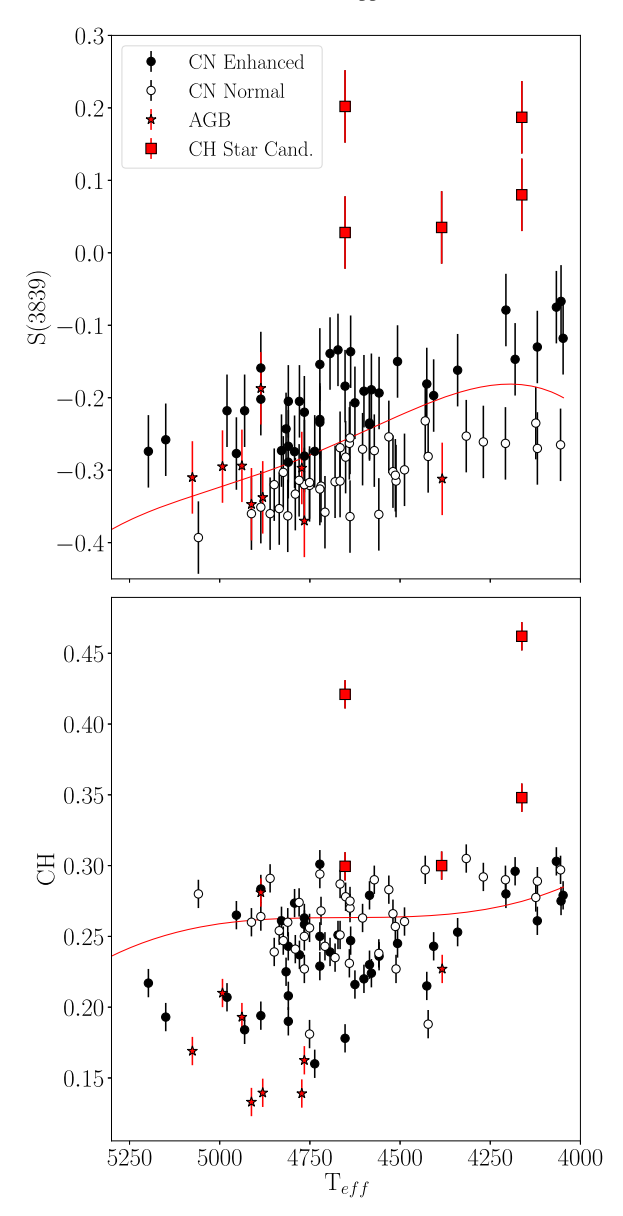


Figure 2. Top panel: CN band strengths as a function of effective temperature for stars in our sample for M53. The red line shows the fiducial used to determine the δ CN index strength, and identify a star as CN-enhanced (filled) or CN-normal (open). AGB stars are indicated as red stars, RGB stars are shown as circles (filled or open), and CH star candidates are shown as red squares. Bottom panel: CH band strengths as a function of effective temperature using the same symbols as in the upper panel. The same fiducial calculated for CH band strength is also shown. Both bands show a clear trend in temperature.

[O/Fe] values for each star are used. We adopted the [O/Fe] value from Boberg et al. (2016) for the 23 stars with measurements. If [O/Fe] was not measured for the star, we assumed an [O/Fe] of 0.3 dex for CN-enhanced stars and 0.47 dex for CN-normal stars, which are the average values for each population based on the O abundances from Boberg et al. (2016). This method provides more accurate results than assuming a single average [O/Fe] value for the entire sample, because Boberg et al. (2016) shows a 0.6 dex range in O abundances in the cluster. Making an accurate assumption for the [O/Fe] value is important because differences in O abundances of 0.3 dex can cause changes in the final C and N abundances of up to 0.2 dex in fainter, warmer stars.

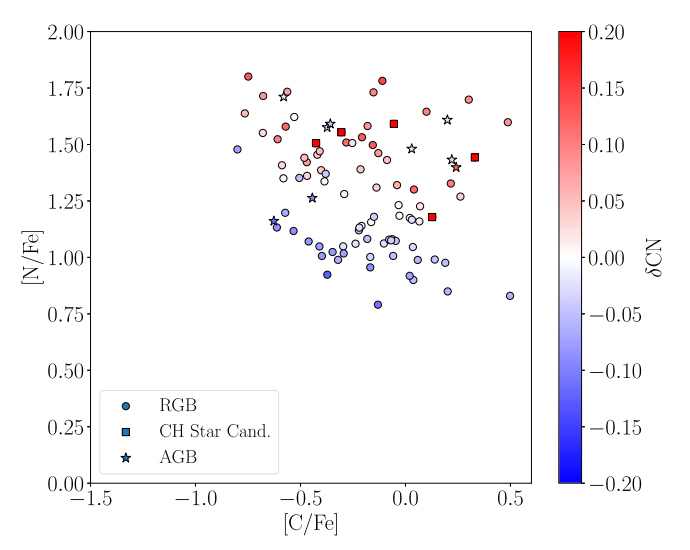


Figure 3. [N/Fe] vs. [C/Fe] for all of the members in our sample in M53. Following the same convention as previous figures, AGB stars are indicated as stars, and the candidate CH stars from Figure 2 are indicated as squares. Points are color-coded based on their δ CN index as indicated by the color bar on the right side of the plot.

The uncertainties in these abundance determinations were calculated using the same method outlined in G18. We adjust the temperature by 150 K, change the [O/Fe] of the CN-enhanced and CN-normal stars, and increase and decrease the S(3839) and CH bands, respectively, by their uncertainties. We add the resulting changes to [C/Fe] and [N/Fe] in quadrature and find uncertainties of 0.2–0.25 dex for each abundance for stars with $M_{\rm V} \leqslant 0$. Fainter stars are found to have slightly higher uncertainties of 0.35 dex, which is mostly due to the CN bands' loss of sensitivity to changes in abundance. A more detailed discussion on our uncertainties using this method can be found in G18.

Figure 3 shows our final derived [C/Fe] and [N/Fe] measurements for each star color-coded by their δ CN values. As expected, we find a spread in C and N with values in the abundance of each element having a range of 1.0 dex or more. This result is similar to what G18 observed in M10, although for M53, the [N/Fe] values are slightly higher than those measured for M10. CN-enhanced and CN-normal RGB stars also map directly onto enhanced and normal N abundances, respectively. Unlike what was found in M10 by G18, Figure 3 shows that the RGB stars in M53 do not separate cleanly into two populations in the C–N plane, but rather show a large range of C and N abundances in each population. Further comparison with M10 shows that while the range in [C/Fe] in the two clusters is roughly the same, the range in [N/Fe] in M53 (1 dex) is smaller than that observed in M10 (\sim 2 dex).

The distribution in Figure 3 and large range in abundances is influenced strongly by evolutionary processes. Because of M53's distance and therefore relatively fainter apparent magnitude compared to other clusters, our sample consists of stars that are mostly above the LFB ($M_{\rm V}=0.168$; Nataf et al. 2013). Since almost all stars in our sample are brighter than the LFB, they have an underlying dependence of abundance on stellar magnitude, with brighter stars having lower C and enhanced N. This effect works to smooth any initial differences in abundance between the CN-enhanced and CN-normal populations that would initially show two distinct distributions

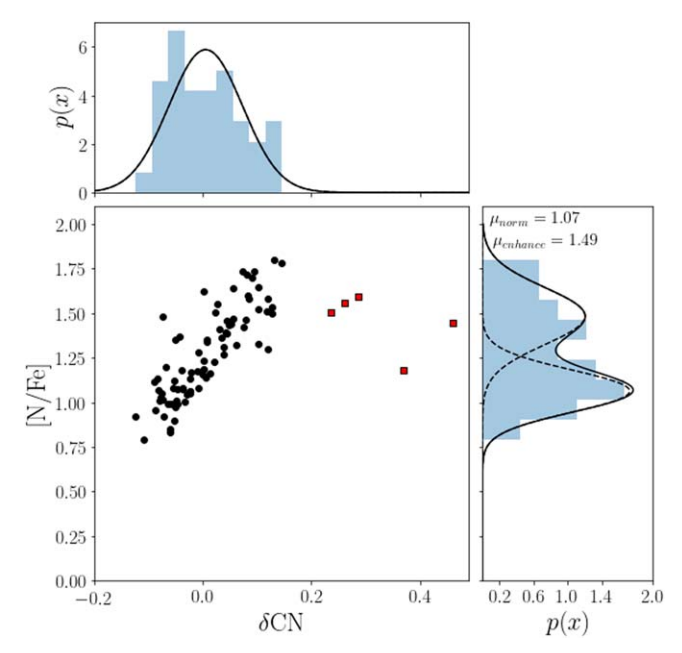


Figure 4. [N/Fe] vs. δ CN for the RGB stars in the sample from M53. CH star candidates are indicated as red squares. Probability distributions for the δ CN and [N/Fe] are shown on the *x*- and *y*-axes, respectively. Data are shown in blue with the two Gaussian distributions yielded by a Gaussian mixture model (GMM) overplotted. The mean values of the fit to the [N/Fe] distribution are given at the top of the histogram. δ CN correlates, as expected, with [N/Fe], and the [N/Fe] distribution shows the clear presence of two distinct populations.

in the C-N plane. We discuss these evolutionary effects further in Section 4.5.

4. Results and Discussion

4.1. Multiple CN Populations in M53

In Figure 4, we plot our δ CN measurements vs. [N/Fe] for all of the RGB stars in our sample. As expected, δ CN correlates with [N/Fe] for the stars in M53. The only exceptions to this correlation are five stars with anomalously high δ CN measurements, which we discuss more fully in Section 4.2. These stars have relatively large δ CN values compared to the rest of the stars in the cluster with all five having δ CN > 0.2. However, we do not find these stars to have significantly larger [N/Fe] measurements than what is seen in the [N/Fe] distribution for the rest of the sample. Because the CN molecular band is dependent on both N and C, the enhanced CN can be equally explained by a high C abundance, and since all of these stars have strong CH bands (as shown in Figure 2), they have relatively enhanced C abundances compared to other stars of similar magnitude (see G18 for a more detailed discussion of how an enhanced CN band does not necessarily imply an enhancement in the underlying N abundance).

The marginal distributions in δ CN and [N/Fe] are also shown in Figure 4 along the x- and y-axes, respectively. While the δ CN index distribution does not allow for a clear separation of multiple populations, the [N/Fe] distribution shows two distinct peaks and confirms the presence of two stellar populations. This figure clearly illustrates the importance of the information from N abundance measurements for the identification of multiple populations in comparison with separation of populations based solely on a δ CN index. Because M53 has such a low metallicity, the difference in δ CN strength between the two populations is too small to easily

distinguish two significant tracks in the S(3839) vs. $T_{\rm eff}$ plot. However, the difference in [N/Fe] between each population becomes clearly distinguishable as two peaks in the distribution. These populations are producing the broad range in CN strength, which is larger than our observational error.

We fit the distribution of [N/Fe], including the stars with high δ CN, with a Gaussian mixture model (GMM). To determine the number of populations to fit to the data, we fit one to ten Gaussians to the distribution and measure the Akaike information criterion (AIC; Akaike 1974) and the Bayesian information criterion (BIC; Schwarz 1978). Using these criteria, we then apply a GMM with two populations, as this number minimized both the AIC and BIC, indicating it was the best fit. The two populations in [N/Fe] are found to have a separation of 0.4 dex and similar standard deviations of 0.13 and 0.16 for the first and second generation, respectively. The separation between populations and the standard deviations do not change significantly when the stars shown with δ CN values greater than 0.2 are excluded. Figure 4 shows the GMM fit to the [N/Fe] distribution. We also show the GMM fit to the δ CN distribution, which does not include the stars with high δ CN. The AIC and BIC indicate that the δ CN distribution is best fit by a single population, which could indicate issues with using δ CN to classify stars into two populations. However, because of the strong correlation between [N/Fe] and our δ CN index, and since a δ CN of 0.0 matches the separating value of 1.28 dex between the two Gaussian distributions for the [N/Fe] distribution, we are confident in our classification by δCN index.

We find that 40 out of 80 of RGB stars in our sample are CN-enhanced based on having a positive δ CN measurement. We do not include in this group the five stars with δ CN > 0.2; these five stars are all classified as CN-enhanced based on their δ CN index, but as seen in Figure 4, these stars are not all N-enhanced. If we calculate the ratio of second-generation stars based on [N/Fe], including all stars, we find that 42 out of 85 of stars are N-enhanced. A value of [N/Fe] equal to 1.28 dex, the midpoint between the two Gaussian curves fit to the [N/Fe] distribution, is adopted to separate the two populations.

4.1.1. AGB Stars

There has been some recent debate over whether or not both populations of stars in GCs evolve onto the AGB. For example, Campbell et al. (2012, 2013) and MacLean et al. (2016) found an absence of the CN-enhanced population on the AGBs in NGC 6257 and M4. These studies suggested that the lack of these stars could be an indication that the He abundance in the second generation of stars is high enough to cause them to skip that phase of stellar evolution. Later studies, however, were able to observe both populations of stars in 47 Tuc, M13, M5, M3, M2, and NGC 6397 (Johnson et al. 2015a; García-Hernández et al. 2015; MacLean et al. 2018), and a recent study by Lagioia et al. (2021) observed both populations of stars in all of the clusters studied. A more detailed review of this debate can be found in G18.

In order to further explore this issue, we have observed AGB stars in M53. However, our final sample of AGB stars in M53 includes only nine stars. Consequently, the conclusions concerning the presence of multiple populations in the AGB phase are not as strong as in our previous studies of M10 and M71 (G18; G20). We also note that our classification of these stars is not as secure as it was for M10 and M71 since the AGB

of M53 is not as clearly defined in the CMD. We present our findings on AGB stars below with this disclaimer in mind.

Our band measurements for the AGB stars in M53 are shown in Figure 2. Based on the S(3839) measurements, the AGB stars in our sample seem to be evenly divided between the CN-enhanced and CN-normal populations with four out of nine AGB stars being CN-enhanced. However, as we discussed in G18, the CN band is dependent on both the C and N abundance, making it important to consider the CH band strength before concluding that a strong or weak CN band is caused solely by N. The lower panel of Figure 2 shows that the AGB stars have relatively weak CH bands (or low C abundances), which will require relatively higher N abundances to explain the CN band strength. This effect explains how AGB stars in Figure 3 with low δ CN values can be found having high [N/Fe] values.

When separating populations by N abundance, we find that seven out of nine AGB stars are N-enhanced. While this ratio does not match that of the RGB stars, our uncertainty in the classification of AGB stars, and our relatively small sample of AGB stars, makes it difficult to make any firm conclusions about whether this difference is a physical result or simply a case of large uncertainties for a small sample. Using a larger sample of stars, Lagioia et al. (2021) found that AGB stars in M53 had a ratio of first-generation to second-generation stars similar to the RGB. Although our study does not have a large enough sample to confirm these results, our analysis shows clear evidence that second-generation (or CN-enhanced) stars are present on the AGB in M53.

4.2. Candidate CH Stars

CH stars are a type of C-enhanced star found along the RGB, and are identified by an extreme level of C-enhancement leading to the presence of unusually strong CH and C2 molecular spectral features. Since these low-mass RGB stars are not expected to have gone through a third-dredge up, the cause of the enhanced C and s-process surface abundances also often seen was a mystery until it was discovered that field CH stars have a binary white dwarf companion (McClure & Woodsworth 1990). Mass transfer due to Roche lobe overflow or stellar winds between the low-mass RGB progenitor and the more massive white dwarf progenitor as it ascended the AGB was then thought to be the cause of these observed abundance peculiarities. This mechanism requires the survival of binaries with semimajor axes large enough to allow the mass transfer to occur during the AGB stage (see, e.g., Côté et al. 1997). However, recent studies have suggested that some species of CH stars with more moderate enhancement may be a result of incomplete CN processing rather than mass exchange (Sharina et al. 2012). It is clear that these objects require further study to understand how they are formed.

CH stars are rarely found in GCs; searches have identified possible CH stars in only ω Cen, M22, M55, M2, M14, M15, and NGC 6426, and these show a range of CH star features (Harding 1962; Dickens 1972; Cowley & Crampton 1985; McClure & Norris 1977; Smith & Norris 1982; Smith & Mateo 1990; Lardo et al. 2012; Côté et al. 1997; Kirby et al. 2015; Sharina et al. 2012). Classic CH stars with strong C₂ bands have only been found in ω Cen and M22 (Harding 1962; Dickens 1972; McClure & Norris 1977; Cowley & Crampton 1985), but in clusters such as M14, M15, and NGC 6426, CH stars with more mild indicators such as strong CH but weak C₂

are observed (Côté et al. 1997; Kirby et al. 2015; Sharina et al. 2012). These differences could be explained by a different formation mechanism such as the incomplete CN processing mentioned above (Sharina et al. 2012), but might also be caused by warmer temperatures that would prevent the formation of strong C_2 bands in their spectra.

In addition to solving issues of formation mechanisms, observing such stars in GCs is important to shed light on the possible connection between the origin of CH stars and the survival and evolution of binary stars in the clusters' dense environments. In order to explore the link between the presence of CH stars and the dynamics of binary stars, Côté et al. (1997) calculated the characteristic value of the semimajor axis, a_h , of surviving binaries in the central regions of GCs; although, as they pointed out, their estimate cannot capture the much more complex evolution of binaries in clusters, it is nevertheless interesting that for several of the clusters in which CH stars have been found, a_h is larger than (or smaller but close to) the value needed for a binary to produce a CH star. Using the values of the central density and velocity dispersion estimated by McLaughlin & van der Marel (2005) for M53, we also find for this cluster that a_h is larger $(a_h \sim 1.86 \text{ au} \text{ and } a_h \sim 2.56 \text{ au}$ using the structural parameters obtained by McLaughlin & van der Marel 2005, respectively, with a King model and a Wilson model fit) than the critical value $(a_h \sim 1 \text{ au})$ adopted by Côté et al. (1997) to determine whether a cluster is likely to host CH stars produced from the evolution of binary stars. In this context, we discuss the identification of potential CH stars in M53.

As noted above, in addition to the two populations of stars separated by S(3839) values in Figure 2, we observed five stars with anomalously high S(3839) measurements and relatively high CH measurements compared to other stars in M53. These stars have radial velocities indicating that they are members. They also all fall along the RGB on the CMD for M53 (see Figure 1) except for one star (ID = 235), which is slightly redder than the RGB for its brightness. Because of their anomalous indices, we made additional checks to guarantee their membership. Three of the stars have more accurate radial velocities through high-resolution spectroscopy from Boberg et al. (2016), and were also confirmed as members based on these radial velocity measurements. We also checked the proper motions of each star as measured by Gaia and found that all five stars have proper motions consistent with the cluster average. One last piece of evidence we have that these stars are true members is the strengths of their Ca H and K bands, which are consistent with other stars in the cluster.

Taking all of this evidence into account, it appears that the index measurements are accurately reflecting members with very strong CN and CH molecular bands. We offer an explanation of these stars below. To aid in our discussion, we have collected parameters of the five stars into a single table, Table 2, which includes magnitudes, stellar parameters, and various abundances such as [C/Fe] and [N/Fe] from this work, and [Na/Fe], [O/Fe], [Ca/Fe], [Ti/Fe], [Ni/Fe], and [Ba/Fe] from Boberg et al. (2016). We also list the δ [C/Fe] and δ [N/Fe] abundances for each star, which are approximations of the initial [C/Fe] and [N/Fe] abundances of the stars before evolutionary changes due to secondary mixing along the RGB altered them (Section 4.5 gives more detail about these changes and how these values are calculated). These corrected C and N abundances allow us to compare stars in similar stages

Table 2 CH Star Candidates in M53

\mathbb{ID}^a	V^1	$(B-V)^{\mathbf{a}}$	R/R_h	M_V^{b}	$T_{e\!f\!f}$	logg	[C/Fe]	$\delta [C/Fe]$	[N/Fe]	$\delta [N/Fe]$	[Na/Fe] ^c	$[{ m O/Fe}]^{ m c}$	[Ca/Fe] ^c	${ m [Ti/Fe]}^{ m c}$	$[\mathrm{Ni}/\mathrm{Fe}]^3$	$[\mathrm{Ba}/\mathrm{Fe}]^3$	P-branch ^d P-branch
18	14.01	1.32	0.998	-2.31	4162	0.86	-0.31	0.27	1.55	1.44	0.2	0.4	0.32	0.18	0.04	0.40	١
26	14.08	1.32	0.921	-2.24	4162	0.89	0.13	69.0	1.18	1.07	:	:	:	:	:	:	yes
47	14.52	1.07	0.796	-1.80	4385	1.22	-0.43	0.03	1.51	1.42	0.3	0.1	0.39	0.31	0.05	0.20	ou
149	15.58	0.92	2.638	-0.74	4652	1.80	-0.06	0.16	1.59	1.55	:	:	:	:	:	:	weak
235	15.96	0.92	2.165	-0.36	4652	1.95	0.33	0.45	4.	1.42	:	:	:	:	:	:	yes
Cluster Med.							-0.18	0.05	1.27	1.23	0.0	0.4	0.36	0.20	-0.05	0.10	

Notes.

^a Rey et al. (1998).

^b Assumes $(m-M)_v=16.32$ (Harris 1996; 2010 edition).

^c Boberg et al. (2016).

^d Indicates the presence of the P-branch of the CH band.

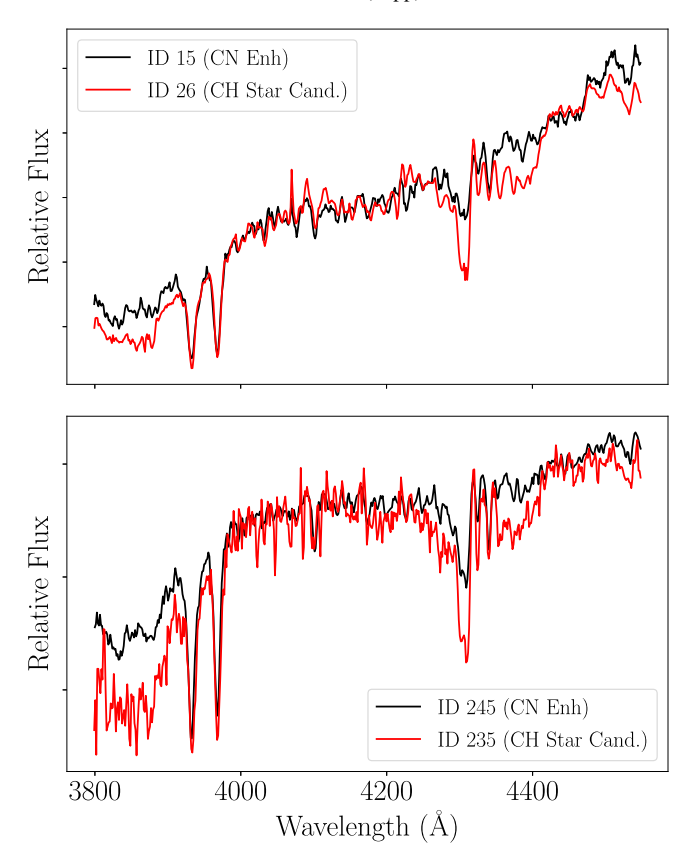


Figure 5. The spectra for the two stars in our sample with the highest S(3839) measurements are plotted in red (ID = 26 and ID = 235, top and bottom panels, respectively). For comparison, stars with similar effective temperatures are also plotted in black (ID = 15 and ID = 245).

of evolution, an important factor for stars that range significantly in magnitude along the giant branch, and where C-depletion of up to 1.0 dex can occur. Table 2 also lists the cluster median among the RGB stars in M53 to give an easy comparison point.

The spectra of the two stars with the highest S(3839) and CH index measurements, ID = 26 and 235, are shown in Figure 5 where we also plot typical CN-enhanced stars of a similar temperature for comparison. The CN and CH molecular features at 3883 Å and 4300 Å are much stronger than the typical CN-enhanced star of a similar temperature. These spectra show the presence of a strong P-branch of the CH band (as indicated in the last column of Table 2), which is visible immediately redward of the CH band at 4300 Å. They also show the appearance of C2 bands (Swan bands) between 4500 Å and 5600 Å. Based on the presence of these features and the high C-enhancement, these two stars are strong candidates to be CH stars (see Keenan 1993, for an example of a classification system of C stars). We also note, as seen in the summary of properties in Table 2, that these two stars have the largest enhancements in [C/Fe] among the possible CH stars.

The other three stars do not show C_2 features as seen in ID=26 and 235, but the P-branch of the CH band is still present in stars ID=18 and 149, although it is weaker than those shown in Figure 5. In addition, these stars are both relatively enhanced in C as indicated by their $\delta[C/Fe]$ values, and ID=18 is also slightly enhanced in the s-process element, Ba, compared to the cluster median. The presence of the P-branch and lack of C_2 features in these stars is similar to what

is found in "weak CH stars" that have been identified in clusters such as M14 and NGC 6242 (Côté et al. 1997; Sharina et al. 2012). Sharina et al. (2012) suggests that these CH stars with more moderate enhancement may be those that go through a different formation scenario where the enhancements are a result of incomplete CN processing as mentioned above. The final star of the five in the sample with δ CN > 0.2 is ID = 47. This star is the weakest candidate to be a CH star as it shows no evidence of C₂ bands or the P-branch, and is not strongly enhanced in C or Ba. However, its CH measurement is still on the high side of the distribution for its given $T_{\rm eff}$, so we have left it in the sample of five possible CH stars due to its relatively high CN and CH band measurements.

Further studies of the s-process elements of these stars would be able to test and confirm whether or not they are true CH stars that have gone through some sort of interaction and mass exchange. If these stars are confirmed as CH stars, some explanation would be needed for how so many of them were found in one cluster. It could be a result of our large sample size in a cluster with the parameters necessary to allow surviving binaries to evolve into CH stars as described above. However, such speculation should be left until these candidate CH stars are confirmed with future high-resolution spectroscopy observations.

4.3. Spatial Distribution of Multiple Populations

Since our sample in M53 covers a broad range in distances from the cluster center, from 0.576 to 6.46 half-light radii (using $R_h = 1.31$; Harris 1996; 2010 edition), we are able to study the spatial distributions of the two populations that we identified. Current formation models of multiple populations predict that second-generation stars form in a more centrally concentrated distribution than first-generation stars (see, e.g., D'Ercole et al. 2008; Decressin et al. 2007a, 2007b; Bekki 2010; Calura et al. 2019). However, dynamical evolution causes the populations to become more spatially mixed over time. Specifically, relaxation-driven mass loss has a large effect on whether or not the populations of a cluster will be spatially mixed. Vesperini et al. (2013) found that unless a cluster had lost at least 60%-70% of its initial mass due to the effects of relaxation, it would still show evidence of the second generation being more centrally concentrated than the first.

M53 has a long relaxation time ($\log(t_{rh}) = 9.76$; Harris 1996; 2010 edition), is currently located at a large galactocentric distance ($R \sim 18.4 \,\mathrm{kpc}$; Harris 1996; 2010 edition), and estimates of its orbital parameters based on Gaia data suggest that it never moves close to the central regions of the Galaxy $(R_{\rm peri} \sim 9 \ {\rm kpc}, R_{\rm apo} \sim 22 \ {\rm kpc};$ Baumgardt et al. 2019). Finally, a recent study by Ebrahimi et al. (2020) has found a steep slope for the stellar mass function in M53 suggesting that the cluster has not been significantly affected by mass loss due to twobody relaxation. These parameters indicate that M53 is unlikely to have suffered a strong internal evolution and mass loss due to two-body relaxation and might thus have preserved some memory of the initial differences between the spatial distribution of first- and second-generation stars (Vesperini et al. 2013). Our analysis of the radial distribution of the ratio of the number of second-generation stars to the total number of stars, shown in Figure 6, does indeed suggest that second-generation stars are more centrally concentrated than first-generation stars. However, a larger number of stars and a broader radial

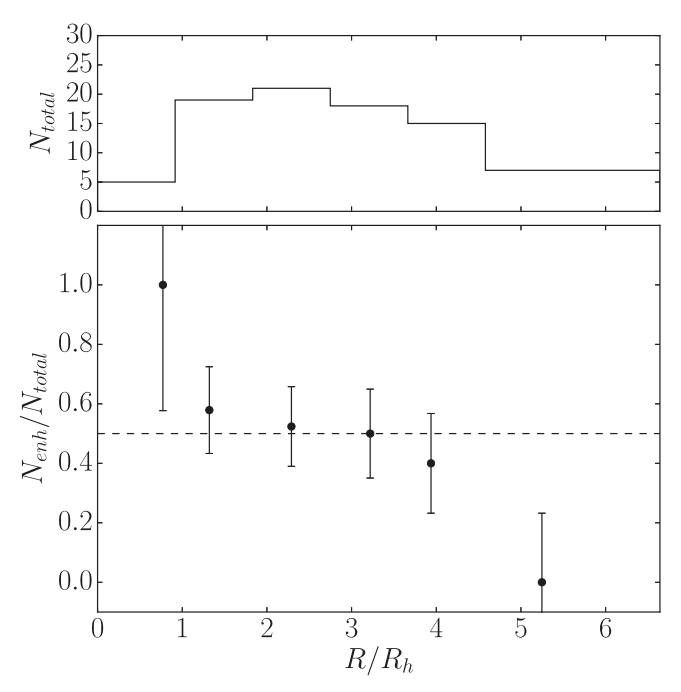


Figure 6. The radial distribution of the ratio of the number of second-generation RGB stars to the total number of RGB stars in M53. To classify stars, we used [N/Fe] = 1.28 dex as the dividing line between populations based on the GMM fit in Figure 4. The top panel shows a histogram of the total number count in each bin. Bin sizes are 1!5 out to 4.5 half-light radii. All stars at a greater radius in our sample are combined into one bin. The points shown in the bottom panel are centered at the average position of the stars in a given radial bin. The error bars for these points reflect the uncertainty in the ratio based on counting statistics. A black dashed line indicates our average ratio for the entire sample.

coverage would be needed to confirm the statistical significance of the trend we found.

Boberg et al. (2016) reached a similar conclusion from the cumulative distribution based on their results separating populations based on Na abundance. Dividing their sample into an inner and outer bin separated at R=3 R_h , we find that the percentage of Na-enhanced stars is 28.4% in the inner bin and 4.8% in the outer bin, indicating a more centrally concentrated second generation. We discuss the differences between the percentage of second-generation stars found by our δ CN identification method and Boberg et al. (2016) in the following section.

4.4. Comparison to Other Methods of Identifying Multiple Populations

4.4.1. Comparison with Na-O Anticorrelation

As mentioned in 2.1, our sample included stars that had observations of Na and O from Boberg et al. (2016), so that we could compare our identification of multiple populations with the identification based on the Na–O anticorrelation. Comparisons between these two classification systems identify outliers, which help constrain theories on multiple population formation. This comparison is also interesting in M53 because Boberg et al. (2016) found three stars in their sample to be Nanormal, but CN-enhanced based on δ CN values from Martell et al. (2008a). We wanted to explore if these outliers continued to exist with updated measurements of δ CN and [N/Fe], and if additional Na-normal, CN-enhanced stars would be found in a larger sample of stars.

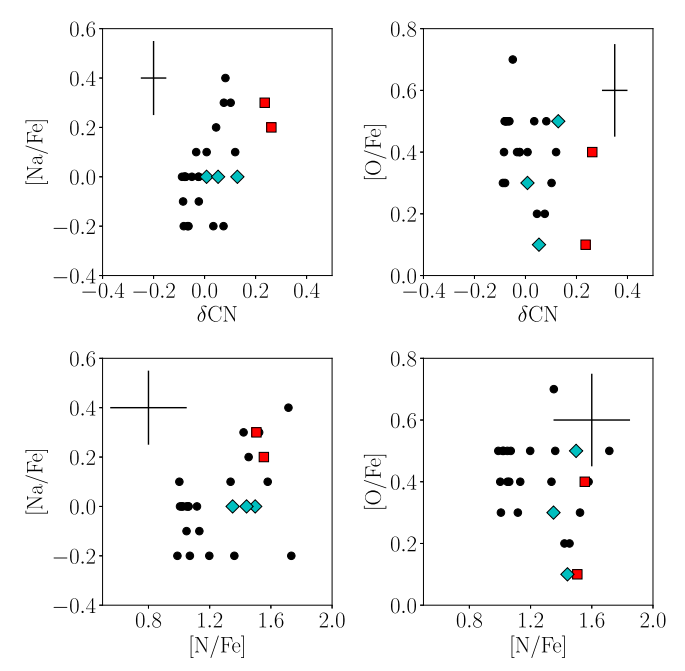


Figure 7. Top panel: [Na/Fe] and [O/Fe] vs. δ CN (left and right, respectively). Na and O measurements are from Boberg et al. (2016). Bottom panel: same as above vs. [N/Fe]. RGB stars are shown as black circles, and CH star candidates are shown as red squares. Cyan diamonds indicate stars that were identified by Boberg et al. (2016) as stars with possible high N and low Na values. Representative error bars show the uncertainties with each measurement.

We plot [Na/Fe] and [O/Fe] measurements from Boberg et al. (2016) vs. our δ CN and [N/Fe] values in Figure 7. Representative uncertainties are also shown in each panel. A general correlation between N-Na and an anticorrelation between N-O is observed as expected, although neither relation is very tight due to the relatively large uncertainties in such a low-metallicity cluster. We note that there are some stars with intermediate [Na/Fe] values and slightly enhanced δ CN or [N/Fe] values. Included among these stars are the three stars observed by Boberg et al. (2016) to have high δ CN and low [Na/Fe], which are indicated as blue diamonds in Figure 7. In addition, we find two stars with [Na/Fe] as low as -0.2 dex that are found to have enhanced δ CN and [N/Fe] values. However, none of these stars deviate from the correlation by more than 1σ , which makes it difficult to draw strong conclusions about whether or not they indicate a population of stars with enhanced N but normal Na abundance. Therefore, our results would indicate that our method using CN band analysis to identify multiple populations and the analysis using the Na-O anticorrelation are in general agreement with one

While the Na, O, and N values are in general agreement, Boberg et al. (2016) found a different ratio between first- and second-generation stars than we do. Thirteen stars were identified as second generation out of their total sample of 49 stars, which gives 27% (compared to our 50%). Other studies have also found that the ratio between populations in clusters does not match what is found when stars are sorted using the Na–O anticorrelation. For example, in a study of 12 GCs, Pancino et al. (2010) found that all clusters studied had a higher percentage of first-generation stars compared to what was observed using the Na–O anticorrelation. Smith et al. (2013) and Smith (2015) also observed stars in M5 and 47 Tuc that

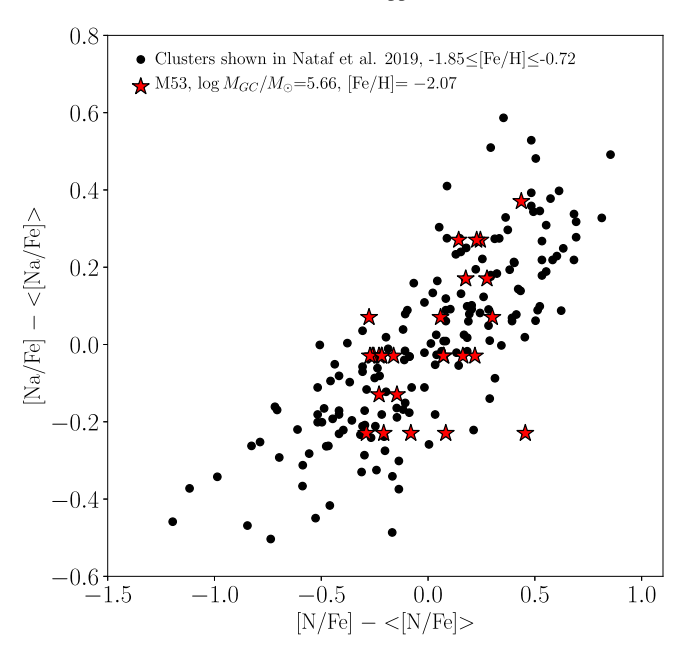


Figure 8. Figure 19 from Nataf et al. (2019) with our data for M53 plotted as red stars. The x-axis shows the difference between [N/Fe] for each star and the average [N/Fe] for the cluster, and the y-axis shows the same for Na. M53 shows a similar correlation as the other clusters, which agrees with the results of the analysis of Nataf et al. (2019) showing that this correlation is independent of cluster mass.

were Na-normal, but CN-enhanced, and vice versa (in the case of M5). Anomalous stars such as these could explain the differences in percentage of first-generation stars based on the identification method seen in Pancino et al. (2010).

However, in the case of M53, the discrepancy between the ratio of first- and second-generation stars likely comes from the fact that the [Na/Fe] distribution, as seen in Figure 6 of Boberg et al. (2016), is more continuous than the [N/Fe] distribution. This means that the two populations do not separate clearly in the Na–O plane as they do in the [N/Fe] distribution. We also note that moving the separating line in [Na/Fe] from 0.2 dex, which was used by Boberg et al. (2016) to distinguish populations, to 0.0 dex would bring the ratio in line with our 50%. In addition, the average uncertainties of the [Na/Fe] measurements are 0.15 dex, and lead to greater uncertainties in classification. These factors, along with the smaller sample size used by Boberg et al. (2016), could explain how different ratios would be found.

4.4.2. N-Na Correlation

A recent study by Nataf et al. (2019) compared correlations in N, Na, and Al in a large sample of clusters to determine if the strengths and slopes of these correlations were related to cluster properties such as mass and metallicity. As part of this study, they compared the slope in the correlation between [Na/Fe] and [N/Fe] among clusters of varying total mass and metallicity to test if the slope was related to either of these parameters. They found that the slope does not appear to change from cluster to cluster, which would indicate that it is independent of cluster mass and metallicity. We add our sample in M53 to this study as shown in Figure 8 where we plot $[Na/Fe]-\langle [Na/Fe]\rangle$ vs. $[N/Fe]-\langle [N/Fe]\rangle$ for the stars in M53 (this study) with the values for other clusters from Nataf et al. (2019; see references therein). $[x/Fe]-\langle [x/Fe]\rangle$ is simply

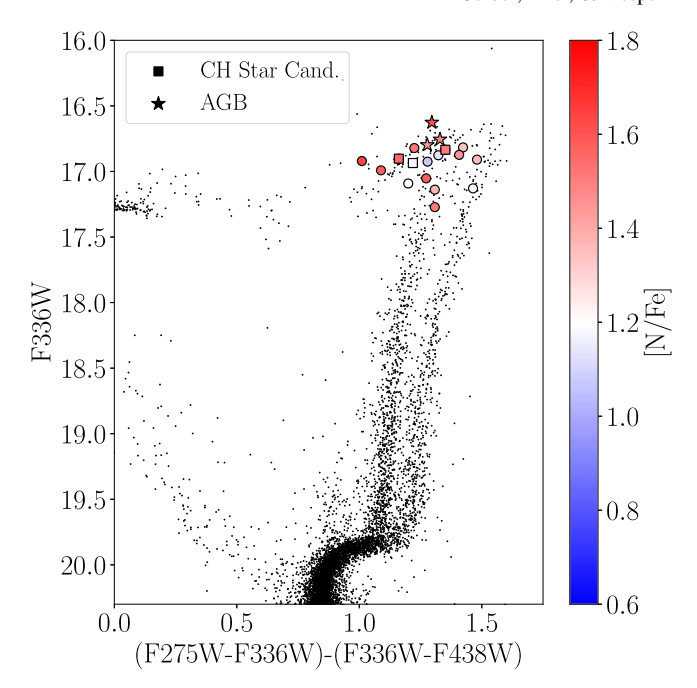


Figure 9. A pseudo-CMD (Piotto et al. 2015; Nardiello et al. 2018) to determine multiple populations photometrically shown with stars color-coded based on [N/Fe]. RGB stars are shown as circles, AGB stars as stars, and candidate CH stars as squares. The pseudo-color enhances the separation between the red giant branches of the populations in the cluster, but the sequences become confused at the brightest magnitudes.

the value for N or Na for a star subtracted by the average value for the cluster. As in Nataf et al. (2019), these values are calculated to compensate for the difference in [Fe/H] between the clusters, and to put all of the measurements on approximately the same scale for better comparison. Figure 8 shows that the slope in the correlation between Na and N for M53 generally agrees with those observed for other clusters considering the uncertainties in our measurements and those in [Na/Fe]. Our results for M53 then support the conclusion of Nataf et al. (2019) that the slope in the correlation between N and Na appears to be independent of cluster mass and metallicity.

4.4.3. Comparison with HST UV Legacy Archive Photometry

HST UV photometry has been used to identify multiple populations in M53 by Milone et al. (2017). This method makes use of pseudo-colors, or different combinations of colors, that enhance the separation between the populations in a cluster because they are dependent on C, N, and O abundances of a star (see Piotto et al. 2015; Milone et al. 2017). A "pseudo-CMD" created using one of these pseudo-colors shows distinct RGB sequences, where the second-generation stars rich in N appear "bluer" and the first-generation stars, with lower N, appear "redder."

Using HST photometry from Piotto et al. (2015) and Nardiello et al. (2018), we re-create the pseudo-CMD in M53 to make a comparison between our method of identifying multiple populations and the method used by Milone et al. (2017). We have only 19 stars in common with the data from the HST photometry because the HST photometry covers a much narrower field than our data. Figure 9 shows these 19 stars color-coded by [N/Fe] strength overplotted on the pseudo-CMD. The brighter, cooler stars along the RGB in

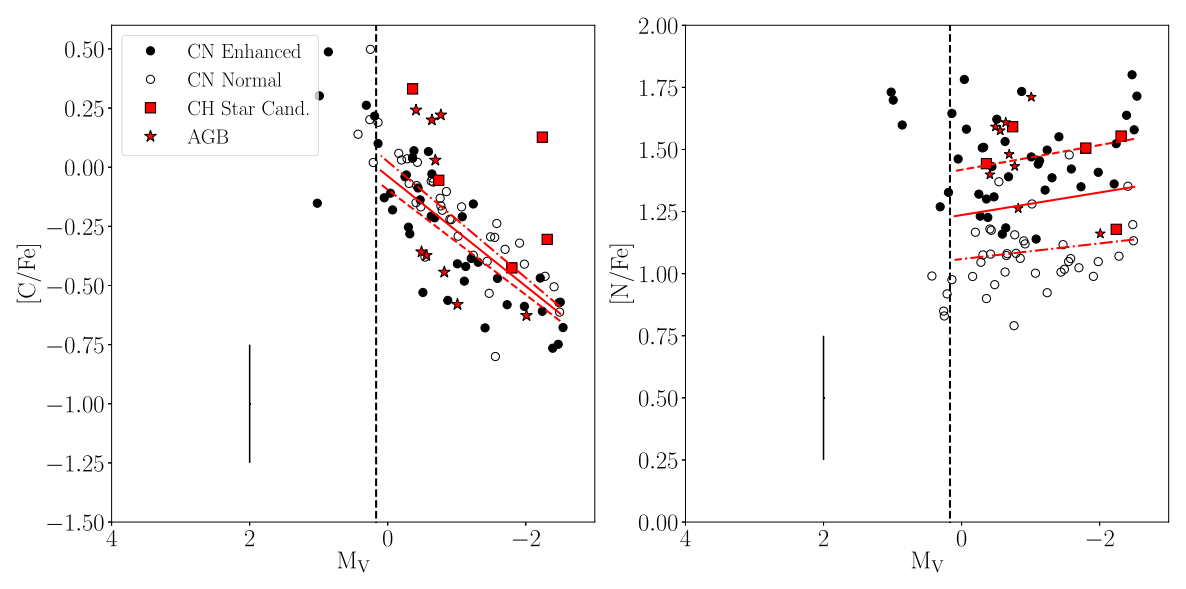


Figure 10. [C/Fe] and [N/Fe] vs. M_V for all 94 member stars in M53. Stars are coded based on their δ CN, with CN-enhanced stars shown as filled circles, and CN-normal stars shown as open circles. AGB stars are shown as red stars, and CH star candidates as red squares. A dashed line at $M_V = 0.0168$ represents the LFB (Nataf et al. 2013), where secondary mixing is expected to begin for this cluster. Linear fits to RGB stars are shown in red for CN-normal, CN-enhanced, and both populations as dotted–dashed, dashed, and solid lines, respectively. Representative error bars are shown in the bottom right of each plot.

the pseudo-CMD move to the "blue," and the RGB bends over as their magnitudes in these HST UV filters become very faint. Essentially, these cool, red stars are not bright enough in the bluer passbands of the near-UV filters to allow for an accurate enough measurement of their pseudo-color to confidently sort them into populations. Unfortunately, because the HST photometry goes much deeper than our sample, the stars in common are some of the brightest in the HST photometry. Therefore, most of our stars with HST photometry fall in a location where the two RGB sequences are no longer distinguished. The faintest four stars in common with the HST photometry appear to fall on the correct RGB sequences, but we are unable to make a strong conclusion about the other RGB stars in our sample with HST photometry. We also do not have enough AGB stars in common with the HST photometry to make any strong conclusions about their locations.

Milone et al. (2017) finds the cluster to be $67\pm2\%$ second-generation stars over their radial distance of 1.35 half-light radii. From Figure 6, we find that the ratio of CN-enhanced stars is around 70% out to this radial distance, consistent with the result from Milone et al. (2017) within the same radius. In Section 4.3, we showed that the second generation is more centrally concentrated in M53, which explains why the percentage of second-generation stars found by Milone et al. (2017) differs from the global value calculated here using the total sample covering a wider radial range.

4.5. Effect of Evolution on C and N Abundances

RGB stars in GCs brighter than the LFB have been shown to have decreasing surface C abundances and increasing surface N abundances as a function of magnitude. Previous studies have tried to constrain the rate of C-depletion by studying the brightest RGB stars in GCs and determining a rate based on an assumed initial C abundance (Martell et al. 2008b; Gerber et al. 2019). However, because these stars can be observed to have a large range of initial C abundances, these studies have struggled to calculate precise C-depletion rates.

We avoid these issues and can determine a more precise C-depletion rate in M53 due to our large sample size covering a range in magnitudes from the LFB to the tip of the RGB. Our sample allows for each population in M53 to be analyzed independently to make comparisons. To determine a rate of mixing for M53, we use a simple linear-least-squares regression for our entire sample that begins at the LF bump measured to be $M_{\rm bump} \sim 0.02$ by Nataf et al. (2013). We also fit the change of [C/Fe] and [N/Fe] as a function of magnitude for the CN-enhanced and CN-normal populations independently. We do not include the AGB stars or candidate CH stars in our sample in any of these fits.

Figure 10 shows the results of these fits overplotted on [C/Fe] and [N/Fe] vs. M_V for our sample. CN-enhanced stars are indicated as filled circles and CN-normal stars as open circles. Because M53 is a relatively distant and faint cluster, we were not able to observe many stars before the LFB to efficiently constrain the initial C and N abundances of stars before mixing occurs, which means we cannot comment on the whether or not there is pre-LFB bump mixing as reported by Angelou et al. (2012). However, we are still able to determine the rate of depletion because we did observe stars faint enough to reach the LFB and capture the range of magnitudes over which stars are mixing in M53.

Our analysis shows that both populations in M53 have similar C-depletion and N-enhancement rates, which indicates similar mixing efficiencies. For the CN-enhanced population, we find a C-depletion rate of 0.22 ± 0.03 dex mag⁻¹, and for the CN-normal population, we find a depletion rate of 0.25 ± 0.03 dex mag⁻¹. For [N/Fe], we find enhancement rates of -0.05 ± 0.03 dex mag⁻¹ and -0.03 ± 0.04 for the CN-enhanced and normal populations, respectively. We list these rates in Table 3.

Since the rates for the change in [C/Fe] and the change in [N/Fe] for each of the two populations are consistent within the uncertainties, we conclude that both populations are mixing at the same rate. This result agrees with our earlier results for M10 where both populations also had depletion rates that agreed

Table 3
Rate of Abundance Change vs. Magnitude for M53 and M92

$d[C/Fe]/dM_V$	$d[N/Fe]/dM_V$
0.23 ± 0.02	-0.05 ± 0.04
0.22 ± 0.03	-0.05 ± 0.03
0.25 ± 0.03	-0.03 ± 0.04
0.253 ± 0.023	
	$0.23 \pm 0.02 \\ 0.22 \pm 0.03 \\ 0.25 \pm 0.03$

Note.

within uncertainties. While the rates of C-depletion do not match the inverse rate of N-enhancement, this discrepancy can be explained by the logarithmic nature of the [N/Fe] and [C/Fe] measurements and the fact that the stars have much higher levels of N than C. For example, consider a parameter whose value changes by 3. If the difference is from 1 to 4, then on a log scale, the parameter ranges from 0 to 0.6 dex, but if the difference is from 10 to 13, on a log scale, it is only 0.11 dex.

Once we calculate the rates of change for C and N, we apply these rates to our abundances to estimate what a star's initial abundance would have been before experiencing extra mixing. Normalized $\delta[\text{C/Fe}]$ and $\delta[\text{N/Fe}]$ measures for each star are created by using the linear fits to [C/Fe] and [N/Fe] vs. magnitude to correct for these evolutionary effects. These corrected abundances are shown in Figure 11, and can be used to study the C–N anticorrelation in RGB stars before the evolutionary effects act on abundances. In Figure 11, the two populations now show a clearer separation in the C–N plane compared to Figure 3. It also seems that the second generation shows a larger spread in initial C and N abundances than the first generation.

In addition, we compare our data to similar data sets of C abundances for M92 as compiled by Smith & Martell (2003) from various literature sources, and for three low-metallicity GCs studied by Kirby et al. (2015; NGC 2419, M68, and M15). We chose these clusters because they have comparably sized data sets in the literature, and because of their similar age and metallicity to M53. Because these clusters have similar metallicities, most theories of extra mixing predict that they should have similar mixing efficiencies.

Smith & Martell (2003) found a value of 0.25 ± 0.02 dex mag⁻¹ overall for the [C/Fe] measurements in M92, which agrees well with what we find for M53 $(0.23 \pm 0.02 \text{ dex})$ mag⁻¹). Kirby et al. (2015) fit NGC 2419, M68, and M15 simultaneously since all were found to have similar rates of C-depletion, and found a depletion value of d[C/Fe]/ $d \log(L/L_{\odot}) = -0.82 \pm 0.02$. On the same $\log(L/L_{\odot})$ scale, our C-depletion rate for the entire M53 sample of RGB stars is $d[C/Fe]/d \log(L/L_{\odot}) = -0.50 \pm 0.05$. While the rate of depletion for M53 is lower than what was found in clusters of similar metallicity by Kirby et al. (2015), we note that Kirby et al. (2015) did not separate stars by population in two of the three clusters that they studied (M68 and M15), which make up a bulk of their sample. If their sample in either of these clusters happened to include more second-generation stars than first-generation stars at the brighter luminosity end or more

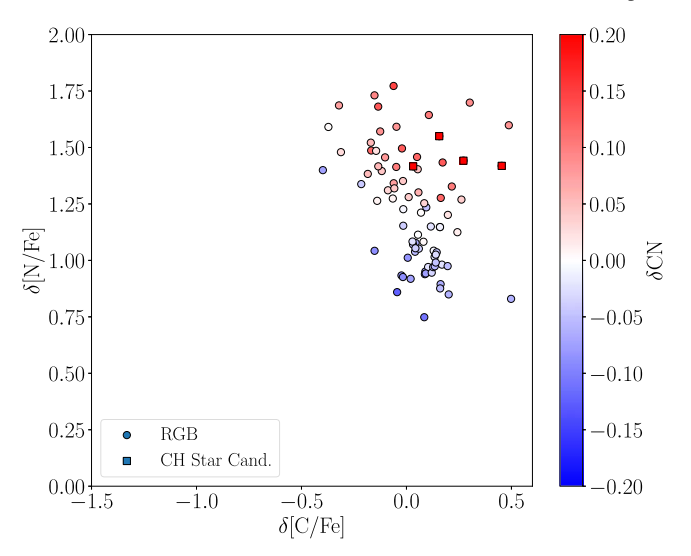


Figure 11. δ [N/Fe] vs. δ [C/Fe] for RGB stars in our sample created by removing the trends in abundance found with magnitude, which are shown in Figure 10. The color convention is the same as that used in Figure 3.

first-generation stars than second-generation stars at the lower luminosity end (or both), then the slope of the fit to the C-depletion rate could end up skewed toward a more negative value, since second-generation stars have lower initial C abundances than first-generation stars. This effect could be enough to explain the difference in depletion rates between the two fits to samples of RGB stars from GCs with similar metallicities.

4.5.1. C+N+O Abundances

We study the C+N+O abundance of each population in M53 by combining our C and N abundances with the O abundance from Boberg et al. (2016), and we compare it with similar measurements in M10 using the values from G18. The left panel of Figure 12 shows the calculated [C+N+O/Fe] vs. $M_{\rm V}$ for all of the stars in our sample with O abundances. We find that the second generation has a higher C+N+O abundance than the first generation with a separation of roughly 0.2 dex (see D'Antona et al. 2016, for models predicting possible C+N+O differences similar to this value). The second generation has an average [C+N+O/Fe] value of 0.53 ± 0.09 (std) dex, and the first generation has an average of 0.33 ± 0.08 (std) dex. A student test on the hypothesis that the [C+N+O/Fe] samples for both populations were pulled from a distribution with the same mean resulted in a p-value of 1×10^{-5} , which indicates that the two populations have significantly different [C+N+0/Fe] abundances.

These results for the [C+N+O/Fe] in each population in M53 are comparable to what we observed in M10 using our C and N measurements and the O abundances from the literature (G18 and references therein). In the middle panel of Figure 12, we plot [C+N+O/Fe] for M10 as a function of magnitude. For M10, we find that the second generation has an average value of 0.44 ± 0.11 (std) dex, and the first generation has an average value of 0.28 ± 0.10 (std) dex. We conducted the same student test on the [C+N+O/Fe] values for M10 as we did for M53, which resulted in a p-value of 3×10^{-5} . This p-value indicates that the two populations in M10 also have significantly different [C+N+O/Fe] abundances. The average [C+N+O/Fe] values for

^a Smith & Martell (2003).

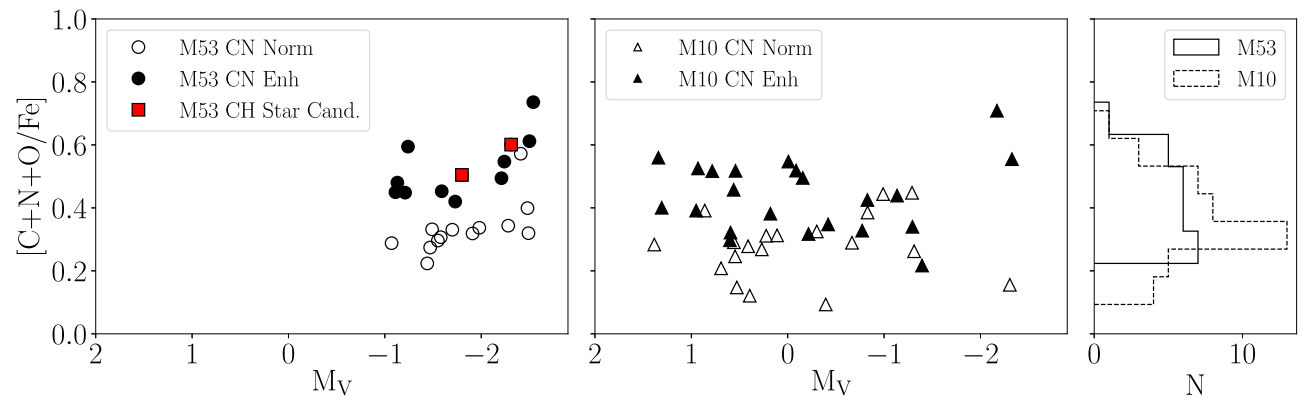


Figure 12. Left panel: [C+N+O/Fe] measurements for RGB stars in our sample in M53 with O abundances from Boberg et al. (2016). The color convention is the same as that used in Figure 2. Middle panel: [C+N+O/Fe] measurements for RGB stars in M10 using data from G18 and O abundances from Carretta et al. (2009a) and Carretta et al. (2009b). Right panel: histograms showing the distributions of both samples. M53 is shown as a solid line, and M10 as a dashed line.

Population	[C+N+O/Fe]	[C+N/Fe]
M53		
CN-enhanced	$0.53 \pm 0.09 \text{ (std)}$	$0.81 \pm 0.15 \text{ (std)}$
CN-normal	$0.33\pm0.08~\text{(std)}$	$0.47 \pm 0.10 \text{ (std)}$
M10 ^a		
CN-enhanced	$0.44 \pm 0.11 \text{ (std)}$	$0.71 \pm 0.21 \text{ (std)}$
CN-normal	$0.28 \pm 0.10 \text{ (std)}$	$0.19 \pm 0.12 \text{ (std)}$

Note.

each population in M10 and M53 are shown in Table 4. The right panel of Figure 12 shows the distribution of C+N+O for each cluster for a direct comparison.

The difference in [C+N+O/Fe] between populations and the standard deviation in each population in M10 is similar to what we measure in M53. Both populations in each cluster also have approximately equal standard deviations. We also note that the C+N+O abundances are not heavily affected by the extra mixing that is causing C-depletion and N-enhancement due to the fact that the material being brought to the surface of the star has been processed through the CN(O)-cycle. Therefore, the C being depleted has been converted into N, which keeps C+N+O constant. We study the C+N abundances to further demonstrate how the sum of these abundances stays constant with increasing luminosity. The left panel of Figure 13 shows the [C+N/Fe] values for all RGB stars in our sample in M53, and the middle panel shows the [C+N/Fe] values for M10, as in Figure 12. From this figure, we find that there is no trend with magnitude for either cluster, as expected. In each cluster, the second generation also has a slightly larger spread in [C+N/Fe] than the first generation, with the populations having standard deviations of 0.15 dex and 0.1 dex, respectively, in M53, and 0.2 dex and 0.1 dex in M10. The dispersions about the mean for the first generation in each cluster are consistent with our uncertainties for [C/Fe] and [N/Fe], while the dispersions for the second generation in each cluster are slightly larger. The mean abundance differences are given in Table 4.

5. Conclusions

In this paper, we focused on measurements of CN and CH band strengths for 85 RGB stars and nine AGB stars in the GC M53. We used these measurements to identify CN-enhanced and CN-normal populations, and calculate C and N abundances for all stars in the sample. The conclusions we reached from this analysis are listed below:

- 1. We find a large spread in CN at a given $T_{\rm eff}$ that indicates the existence of more than one population in the cluster. The populations separate more clearly in the [N/Fe] distribution, which indicates the presence of an N-enhanced and an N-normal population. We find the RGB stars in our sample to be evenly divided between each population.
- 2. We have identified five stars as CH star candidates based on their extremely strong CN and CH bands. Of these, the strongest two candidates have a clear P-branch of their CH band, as well as the slight appearance of molecular C2 features. We have thoroughly checked the membership of these stars with radial velocities determined through high-resolution spectroscopy and proper motions from Gaia. Stellar properties and abundances are presented for these stars in Table 2. Follow-up high-resolution spectroscopy of these stars is necessary to confirm whether these are indeed CH stars that have gone through some sort of interaction with a binary companion. If they are confirmed to be CH stars, having so many in one cluster may require further explanation.
- 3. We compare our method of identifying multiple populations to other methods such as the Na–O anticorrelation (Boberg et al. 2016) and HST UV photometry (Milone et al. 2017). Our method agrees reasonably well with both of these methods. While the correlation and anti-correlation between N–Na and N–O, respectively, are not as tight as they were in M10, this can be explained by the higher uncertainties involved in abundance measurements for a lower-metallicity cluster.
- 4. We find that the second generation (CN-enhanced population) in M53 is more centrally concentrated than the first generation. This result agrees with the conclusions of Boberg et al. (2016) using the Na–O anticorrelation to identify populations. Various dynamical parameters suggest that M53 is not in its advanced evolutionary stages and has not suffered strong mass loss

^a G18 and references therein.

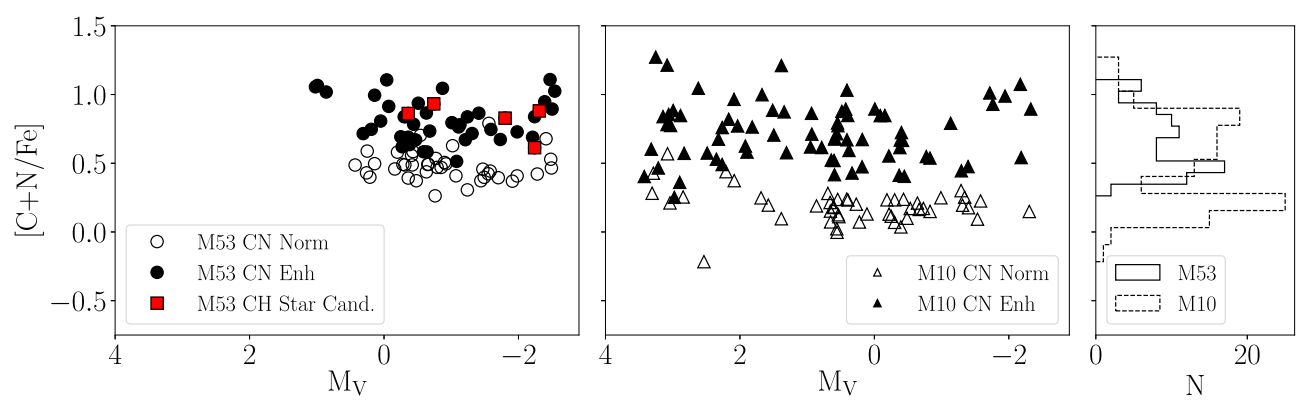


Figure 13. Left panel: [C+N/Fe] measurements for RGB stars in our sample in M53. The color convention is the same as that used in Figure 2. Middle panel: [C+N/Fe] measurements for RGB stars in M10 using data from G18. Right panel: histograms showing the distributions of both samples. M53 is shown as a solid line, and M10 as a dashed line.

due to relaxation, and the presence of a radial gradient in the fraction of second-generation stars is generally consistent with the dynamical models of Vesperini et al. (2013).

- 5. A large range of values is found for both the [C/Fe] and [N/Fe] measurements for the RGB stars, which is expected. Because most of our stars have evolved past the LFB, the magnitude dependence of [C/Fe] and [N/Fe] abundances obscures the distinct populations in the C-N plane. The separation between these two populations becomes clearer once we remove the dependence on magnitude based on our fits to [C/Fe] and [N/Fe] vs. magnitude.
- 6. We calculate [C+N+O/Fe] for stars in our sample that have O abundances from Boberg et al. (2016), and compare to similar measurements in M10 from G18 and references therein. In M53, we find second-generation stars to be enhanced in [C+N+O/Fe] by ~0.2 dex, an enhancement comparable to that found for second-generation stars in M10.
- 7. Our sample of AGB stars is not large enough to draw any strong conclusions about the proportion of second-generation stars found on the AGB in M53. However, we do observe both first- (two) and second- (seven) generation stars on the AGB; so while the ratio in populations may be different from the RGB, neither population is completely absent.
- 8. We determine a rate of change for [C/Fe] and [N/Fe] as a function of M_V for each population to study the evolutionary effects on C and N caused by extra mixing. Each population in M53 has a similar mixing rate for both C and N. Stars in M53 also have a similar depletion rate for C compared to other clusters of similar metallicity, M92 and M15.

We would like to thank Roger A. Bell for making the SSG program available to us. We would also like to thank Zachary Maas and Nicholas Barth for their help in obtaining the stellar spectra during various runs at WIYN. Additionally, we would like to thank Dianne Harmer, Daryl Willmarth, and all of the observing assistants without whom our observations would not have been possible.

This publication makes use of data products from the Two Micron All Sky Survey, which is a joint project of the University of Massachusetts and the Infrared Processing and Analysis Center/California Institute of Technology, funded by the National Aeronautics and Space Administration and the National Science Foundation (NSF). E.V. acknowledges support from NSF grant AST-2009193.

ORCID iDs

Jeffrey M. Gerber https://orcid.org/0000-0001-9583-0004 Enrico Vesperini https://orcid.org/0000-0003-2742-6872

References

```
Akaike, H. 1974, ITAC, 19, 716
Alonso, A., Arribas, S., & Martinez-Roger, C. 1998, A&AS, 131, 209
Alonso, A., Arribas, S., & Martínez-Roger, C. 1999, A&AS, 140, 261
Alonso, A., Arribas, S., & Martínez-Roger, C. 2001, A&A, 376, 1039
Angelou, G. C., Stancliffe, R. J., Church, R. P., Lattanzio, J. C., & Smith, G. H.
  2012, ApJ, 749, 128
Bastian, N., & Lardo, C. 2018, ARA&A, 56, 83
Baumgardt, H., Hilker, M., Sollima, A., et al. 2019, MNRAS, 482, 5138
Bekki, K. 2010, ApJL, 724, L99
Bell, R. A., Paltoglou, G., & Tripicco, M. J. 1994, MNRAS, 268, 771
Boberg, O. M., Friel, E. D., & Vesperini, E. 2016, ApJ, 824, 5
Briley, M. M., Cohen, J. G., & Stetson, P. B. 2004a, AJ, 127, 1579
Briley, M. M., Harbeck, D., Smith, G. H., & Grebel, E. K. 2004b, AJ,
  127, 1588
Busso, M., Wasserburg, G. J., Nollett, K. M., & Calandra, A. 2007, ApJ,
  671, 802
Calura, F., D'Ercole, A., Vesperini, E., et al. 2019, MNRAS, 489, 3269
Campbell, S. W., D'Orazi, V., Yong, D., et al. 2013, Natur, 498, 198
Campbell, S. W., Yong, D., Wylie-de Boer, E. C., et al. 2012, in ASP Conf.
  Ser. 458, Galactic Archaeology: Near-Field Cosmology and the Formation
  of the Milky Way, ed. W. Aoki, M. Ishigaki, & T. Suda (San Fransisco,
  CA: ASP), 205
Carretta, E., Bragaglia, A., Gratton, R., & Lucatello, S. 2009b, A&A, 505, 139
Carretta, E., Bragaglia, A., Gratton, R. G., et al. 2009a, A&A, 505, 117
Chanamé, J., Pinsonneault, M., & Terndrup, D. M. 2005, ApJ, 631, 540
Charbonnel, C., & Zahn, J.-P. 2007, A&A, 467, L15
Chun, S.-H., Kim, J.-W., Sohn, S. T., et al. 2010, AJ, 139, 606
Chun, S.-H., Lee, J.-J., & Lim, D. 2020, ApJ, 900, 146
Cohen, J. G. 1999a, AJ, 117, 2428
Cohen, J. G. 1999b, AJ, 117, 2434
Côté, P., Hanes, D. A., McLaughlin, D. E., et al. 1997, ApJL, 476, L15
Cowley, A. P., & Crampton, D. 1985, PASP, 97, 835
Da Costa, G. S. 2016, in Proc. IAU Symp. 317, The General Assembly of
  Galaxy Halos: Structure, Origin and Evolution, ed. A. Bragaglia
  (Cambridge: Cambridge Univ. Press), 110
D'Antona, F., Vesperini, E., D'Ercole, A., et al. 2016, MNRAS, 458, 2122
```

de Mink, S. E., Pols, O. R., Langer, N., & Izzard, R. G. 2009, A&A, 507, L1

Decressin, T., Meynet, G., Charbonnel, C., Prantzos, N., & Ekström, S. 2007b,

Decressin, T., Charbonnel, C., & Meynet, G. 2007a, A&A, 475, 859

Denissenkov, P. A., & Hartwick, F. D. A. 2014, MNRAS, 437, L21

```
Denissenkov, P. A., & Tout, C. A. 2000, MNRAS, 316, 395
D'Ercole, A., D'Antona, F., Carini, R., et al. 2012, MNRAS, 423, 1521
D'Ercole, A., Vesperini, E., D'Antona, F., McMillan, S. L. W., & Recchi, S.
   2008, MNRAS, 391, 825
Dickens, R. J. 1972, MNRAS, 159, 7P
Ebrahimi, H., Sollima, A., Haghi, H., et al. 2020, MNRAS, 494, 4226
Eggleton, P. P., Dearborn, D. S. P., & Lattanzio, J. C. 2006, Sci, 314, 1580
Eggleton, P. P., Dearborn, D. S. P., & Lattanzio, J. C. 2008, ApJ, 677, 581
Elmegreen, B. G. 2017, ApJ, 836, 80
Forbes, D. A., & Bridges, T. 2010, MNRAS, 404, 1203
García-Hernández, D. A., Mészáros, S., Monelli, M., et al. 2015, ApJL,
  815, L4
Gerber, J. M., Briley, M. M., & Smith, G. H. 2019, AJ, 157, 154
Gerber, J. M., Friel, E. D., & Vesperini, E. 2018, AJ, 156, 6, (G18)
Gerber, J. M., Friel, E. D., & Vesperini, E. 2020, AJ, 159, 50, (G20)
Gieles, M., Charbonnel, C., Krause, M. G. H., et al. 2018, MNRAS, 478, 2461
Gratton, R., Bragaglia, A., Carretta, E., et al. 2019, A&ARv, 27, 8
Gratton, R. G., Carretta, E., & Bragaglia, A. 2012, A&ARv, 20, 50
Gustafsson, B., Edvardsson, B., Eriksson, K., et al. 2008, A&A, 486, 951
Harbeck, D., Smith, G. H., & Grebel, E. K. 2003, AJ, 125, 197
Harding, G. A. 1962, Obs, 82, 205
Harris, W. E. 1996, AJ, 112, 1487
Henkel, K., Karakas, A. I., & Lattanzio, J. C. 2017, MNRAS, 469, 4600
Hubbard, E. N., & Dearborn, D. S. P. 1980, ApJ, 239, 248
Johnson, C. I., Kraft, R. P., Pilachowski, C. A., et al. 2005, PASP, 117, 1308
Johnson, C. I., McDonald, I., Pilachowski, C. A., et al. 2015a, AJ, 149, 71
Johnson, C. I., Rich, R. M., Pilachowski, C. A., et al. 2015b, AJ, 150, 63
Jordi, K., & Grebel, E. K. 2010, A&A, 522, A71
Keenan, P. C. 1993, PASP, 105, 905
Kimmig, B., Seth, A., Ivans, I. I., et al. 2015, AJ, 149, 53
Kippenhahn, R., Ruschenplatt, G., & Thomas, H.-C. 1980, A&A, 91, 175
Kirby, E. N., Guo, M., Zhang, A. J., et al. 2015, ApJ, 801, 125
Kraft, R. P. 1994, PASP, 106, 553
Lagioia, E. P., Milone, A. P., Marino, A. F., et al. 2021, ApJ, 910, 6
Lardo, C., Pancino, E., Mucciarelli, A., et al. 2012, A&A, 548, A107
Lauchner, A., Powell, W. L., & Wilhelm, R. 2006, ApJL, 651, L33
MacLean, B. T., Campbell, S. W., De Silva, G. M., et al. 2016, MNRAS,
  460, L69
MacLean, B. T., Campbell, S. W., De Silva, G. M., et al. 2018, MNRAS,
  475, 257
Marino, A. F., Milone, A. P., Karakas, A. I., et al. 2015, MNRAS, 450, 815
```

```
Martell, S. L., Smith, G. H., & Briley, M. M. 2008a, PASP, 120, 839
Martell, S. L., Smith, G. H., & Briley, M. M. 2008b, AJ, 136, 2522
McClure, R. D., & Norris, J. 1977, ApJL, 217, L101
McClure, R. D., & Woodsworth, A. W. 1990, ApJ, 352, 709
McLaughlin, D. E., & van der Marel, R. P. 2005, ApJS, 161, 304
Milone, A. P., Piotto, G., Renzini, A., et al. 2017, MNRAS, 464, 3636
Naidu, R. P., Conroy, C., Bonaca, A., et al. 2020, ApJ, 901, 48
Nardiello, D., Libralato, M., Piotto, G., et al. 2018, MNRAS, 481, 3382
Nataf, D. M., Gould, A. P., Pinsonneault, M. H., & Udalski, A. 2013, ApJ,
  766, 77
Nataf, D. M., Wyse, R. F. G., Schiavon, R. P., et al. 2019, AJ, 158, 14
Nordhaus, J., Busso, M., Wasserburg, G. J., Blackman, E. G., & Palmerini, S.
   2008, ApJL, 684, L29
Norris, J., Cottrell, P. L., Freeman, K. C., & Da Costa, G. S. 1981, ApJ,
   244, 205
Norris, J., & Freeman, K. C. 1979, ApJL, 230, L179
Palacios, A., Charbonnel, C., Talon, S., & Siess, L. 2006, A&A, 453, 261
Palmerini, S., Busso, M., Maiorca, E., & Guandalini, R. 2009, PASA, 26, 161
Pancino, E., Rejkuba, M., Zoccali, M., et al. 2010, A&A, 524, A44
Pavlenko, Y. V., Jones, H. R. A., & Longmore, A. J. 2003, MNRAS, 345, 311
Piotto, G., Milone, A. P., Bedin, L. R., et al. 2015, AJ, 149, 91
Prantzos, N., & Charbonnel, C. 2006, A&A, 458, 135
Rey, S.-C., Lee, Y.-W., Byun, Y.-I., et al. 1998, AJ, 116, 1775
Schwarz, G. 1978, AnSta, 6, 461
Sharina, M., Aringer, B., Davoust, E., et al. 2012, MNRAS, 426, L31
Skrutskie, M. F., Cutri, R. M., Stiening, R., et al. 2006, AJ, 131, 1163
Smith, G. H. 2015, PASP, 127, 825
Smith, G. H., & Martell, S. L. 2003, PASP, 115, 1211
Smith, G. H., & Mateo, M. 1990, ApJ, 353, 533
Smith, G. H., Modi, P. N., & Hamren, K. 2013, PASP, 125, 1287
Smith, G. H., & Norris, J. 1982, ApJ, 254, 149
Smolinski, J. P., Martell, S. L., Beers, T. C., et al. 2011, AJ, 142, 126
Suntzeff, N. B., & Smith, V. V. 1991, ApJ, 381, 160
Sweigart, A. V., & Mengel, J. G. 1979, ApJ, 229, 624
Trefzger, D. V., Langer, G. E., Carbon, D. F., et al. 1983, ApJ, 266, 144
Vasiliev, E. 2019, MNRAS, 484, 2832
Ventura, P., D'Antona, F., Mazzitelli, I., & Gratton, R. 2001, ApJL, 550, L65
Vesperini, E., McMillan, S. L. W., D'Antona, F., & D'Ercole, A. 2013,
      NRAS, 429, 1913
Yong, D., Grundahl, F., & Norris, J. E. 2015, MNRAS, 446, 3319
Yuan, Z., Chang, J., Beers, T. C., et al. 2020, ApJL, 898, L37
```